Neuro-Oncology Advances
7(1), vdae215, 2025 | https://doi.org/10.1093/noajnl/vdae215 | Advance Access date 7 December 2024

# Immunocompetent murine glioblastoma stem-like cell models exhibiting distinct phenotypes

**Kimia Kardani, Shanawaz M. Ghouse[#], Muzammil Arif Din Abdul Jabbar[#], Namita Rajasubramanian, Judit Sanchez Gil, Anat Stemmer-Rachamimov, Yasushi Soda, Robert L. Martuza, Toshiro Hara, Hiroaki Wakimoto[*], and Samuel D. Rabkin[*]**

All author affiliations are listed at the end of the article
Present address: Department of Neurosurgery and Biointerfaces Institute, University of Michigan, Ann Arbor, Michigan, USA (T.H.)

[*]Co-senior authors.
[#]Co-second authors.

Corresponding Author: Samuel D. Rabkin, PhD, Department of Neurosurgery, Massachusetts General Hospital, 185 Cambridge Street, CPZN-3800, Boston, MA 02114, USA (rabkin@mgh.harvard.edu).

**Abstract**

**Background**. Glioblastoma (GBM) treatment is hindered by a dearth of representative mouse GBM preclinical models in immunocompetent mice. Here, we characterized 5 murine GBM stem-like cell (mGSC) models derived from lentivirus-induced tumors in transgenic mice that are driven by the activation of the Nf1-Ras signaling pathway and inactivation of Tp53.

**Methods**. MGSC lines (005, RIG, NF53, C1, and C3) were cultured as spheres in serum-free stem cell media. Whole exome sequencing (WES) was employed to quantify single nucleotide polymorphisms (SNPs). Stem cell properties were characterized by stemness in vitro and tumorigenicity after intracerebral implantation in C57BL/6 mice. Tumor phenotypes and the immune microenvironment were characterized by immunohistochemistry, flow cytometry, and RNA sequencing.

**Results**. WES revealed a large variation in coding sequence SNPs across mGSC lines (~20-fold), likely influenced by the mixed backgrounds of the parental mice. MGSCs exhibited variable clonogenic sphere formation and CD133 expression levels. In vivo, they consistently initiated lethal malignant gliomas, with median survival ranging from 29 to 82 days, and showed strong CD44 expression and variable invasiveness. The tumor microenvironment featured an abundance of CD68+ macrophages and uniform high PD-L1+ myeloid cells, while T-cell infiltration varied among the models, with low mutation burden C1 and C3 exhibiting fewer tumor-infiltrating T cells.

**Conclusions**. Upon orthotopic implantation in immunocompetent mice, mGSCs generate tumors characteristic of human GBM. Despite similar strategies to generate these mGSCs, they exhibited a range of phenotypes and immune profiles in mGSC-derived orthotopic tumors. These mGSCs provide new preclinical GBM models for developing GBM immunotherapies.

## Key Points

- New murine glioblastoma stem-like cell models in immunocompetent mice.
- Models exhibited a range of single nucleotide polymorphisms, stemness markers, invasiveness, and immune cell profiles.
- Offer a unique set of representative murine glioblastoma models for immunotherapy research.

## Importance of the Study

The paucity of clinically relevant immunocompetent glioblastoma (GBM) models hampers the preclinical development of immunotherapy strategies and new experimental therapeutics. This study comprehensively characterized 5 murine GBM models that were established as murine GBM stem-like cells (mGSCs) and genetically driven by Ras activation and Tp53 inactivation. Despite similar genetic drivers, these GBM models exhibit a range of aggressiveness (eg, survival times), proliferation, stemness features, and invasiveness in the brain. Of note, flow cytometric analysis of mGSC-derived tumors revealed a dominance of tumor-associated macrophages, recapitulating a hallmark of human GBM. Conversely, the abundance of tumor-infiltrating lymphocytes (TILs) varied substantially, with the 2 mGSCs carrying the fewest single nucleotide polymorphisms demonstrating the lowest TIL levels. Thus, these unique well-characterized mGSC-based GBM models offer much-needed tools for understanding GBM biology, devising immunotherapeutic strategies, and bridging the gap between rigorous laboratory investigations and clinical advances in GBM treatment.

Glioblastoma (GBM) accounts for 50.1% of all malignant primary central nervous system (CNS) tumors in the United States.[1] The newest World Health Organization classification of CNS tumors[2] defines GBM as isocitrate dehydrogenase (IDH)-wildtype, diffuse glioma, grade 4 that is characterized by classic histological hallmarks (ie, necrosis and endothelial proliferation) and/or distinct genetic alterations such as *TERT* promoter mutation, chromosome 7/10 alterations, and *EGFR* amplification. Despite much improved molecular understanding and aggressive multimodal treatment, GBM remains invariably lethal.[1] Recent approval of tumor-treating fields only modestly increased overall survival to 20.9 months.[3] Clinical investigations of exploratory therapeutic modalities for GBM have been largely disappointing,[4] especially immunotherapy strategies like immune checkpoint inhibitors.[5] This highlights the need for robust preclinical research to better understand the biology of GBM and the tumor microenvironment (TME), and the use of immunocompetent clinically relevant disease models.

Orthotopic GBM in rodent brain provides a disease-relevant environment in which neoplastic cells interact with nonneoplastic cells and extracellular matrix in the brain. Human GBM xenografts in immune-deficient mice allow investigations of human tumor cells' responses to therapy. Patient-derived xenografts and patient-derived GBM stem-like cell (GSC)-based xenografts offer the advantage of recapitulating patient-specific molecular alterations and tumor phenotypes.[6,7] We have extensively employed orthotopic GBM models generated with patient-derived GSCs to characterize oncolytic viruses and molecularly targeted agents as anti-GBM therapeutics.[8–12] However, the use of immunodeficient animals for xenografts critically limits studies of immunotherapies that require an intact immune system to mediate antitumor effects. Reconstitution with human immune progenitor cells (humanization) may overcome this problem, but the cumbersome process, lack of complete diversity and accurate reconstitution, and the costs remain a hurdle.[13,14]

Murine GBM cells in immunocompetent mice have served as the mainstream models for GBM immunotherapy research.[15] Two of the most frequently used murine GBM cell lines, GL261[16] and CT2A,[17] are syngeneic to C57BL/6 mice and form highly aggressive GBMs. However, both are chemical carcinogen-induced GBMs[15] with a high mutation burden, and GL261 being immunogenic, making them poorly representative of human GBM.[18,19] Genetically engineered mouse (GEM) models of GBM, in contrast, are generated and driven by specific genetic drivers that are relevant to the pathogenesis of human GBM.[15] GBM cell lines can be established from these murine GBMs and offer transplantable immunocompetent models. 005 GSCs were created by low-level infection of a lentivirus vector containing HrasV12-LoxP in Tp53$^{-/+}$ GFAP-Cre mice[20,21] (Figure 1A). It displays pathological features of GBM (eg, invasiveness and angiogenesis) and characteristics of GSCs, as evidenced by multi-lineage differentiation, stem cell marker expression, nonadherent growth in serum-free media, and neurosphere formation.[20,21] Because of these representative traits as a preclinical GBM model, 005 mouse GSCs (mGSCs) have been increasingly used by investigators, including us, for a variety of research applications such as studies of the TME,[23] exploration of immunotherapeutic strategies,[11,20,24–28] and testing nanoparticle drug deliveries.[29,30]

Khalsa and colleagues utilized RNA sequencing and Cytometry by time of flight to comprehensively profile the immune tumor landscape of murine GBMs including 005, and found that 005 and GL261 were relatively enriched for immune-related gene expression compared with CT-2A and Mut3, while 005 was characterized by a lower frequency of exhausted CD8+ T cells.[31] These findings provide us with an atlas of the immunological phenotypes of commonly used murine GBMs and guidance for selecting models appropriate for specific research needs. However, since the genotypes and mutation burden of these murine models greatly vary, what contributed to an individual tumor's immune profile is unknown. Thus, we herein set out to characterize 5 GEM-derived mGSC-based models of murine GBM that are all driven by activation of the NF1-Ras MAP kinase signaling pathway and inactivation of the tumor suppressor Tp53. While Ras mutations are rare in GBM, activated Ras signaling (MAPK/PI3K) is very common.[32] Despite the similar molecular strategy used to generate these mGSCs, we noted a range of tumor phenotypes and tumor immune microenvironmental profiles.

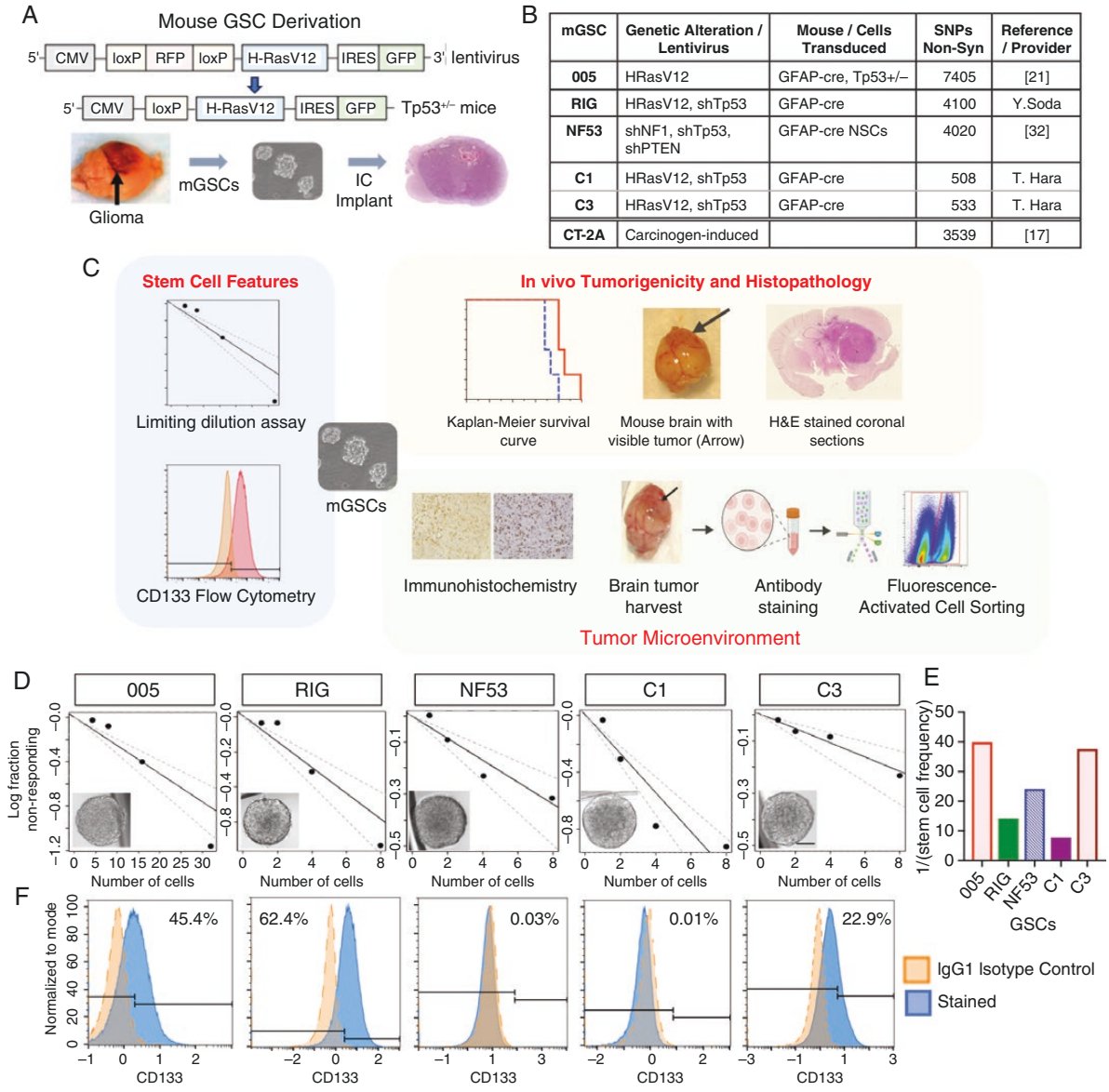


| mGSC | Genetic Alteration / Lentivirus | Mouse / Cells Transduced | SNPs Non-Syn | Reference / Provider |
|---|---|---|---|---|
| **005** | HRasV12 | GFAP-cre, Tp53+/– | 7405 | [21] |
| **RIG** | HRasV12, shTp53 | GFAP-cre | 4100 | Y.Soda |
| **NF53** | shNF1, shTp53, shPTEN | GFAP-cre NSCs | 4020 | [32] |
| **C1** | HRasV12, shTp53 | GFAP-cre | 508 | T. Hara |
| **C3** | HRasV12, shTp53 | GFAP-cre | 533 | T. Hara |
| **CT-2A** | Carcinogen-induced | | 3539 | [17] |

**Figure 1.** Characterization of murine glioblastoma stem-like cell (mGSC) lines. (A) Schematic figure of mGSC derivation starting with an example of H-Ras-GFP lentivirus construct, Cre-mediated recombination, induced glioma isolation, mGSC culture, and implanted tumors. (B) Table of lentivirus-induced genetic alterations, mouse strains used, and the number of non-synonymous (non-syn) single nucleotide polymorphisms (SNPs) determined by whole exome sequencing of each mGSC line and CT2A. (C) Schematic figure of the experimental approaches. Parts created with BioRender. (D) Extreme limiting dilution analysis (ELDA) was used to estimate stem cell frequency for different mGSCs. The x-axis represents the number of cells plated, while the y-axis displays the log fraction of nonresponding wells. Graphs were plotted at https://bioinf.wehi.edu.au/software/elda/.[22] Also shown are representative images of clonogenic spheres (scale bar = 100 mm). (E) ELDA derived 1/stem cell frequency from D. (F) Flow cytometric analysis of neuronal stem cell marker CD133 expression. Dissociated cells were stained either with IgG1 isotype control or anti-CD133 antibody conjugated with phycoerythrin (PE). The percentages of CD133+ cells are indicated in each panel.

## Materials and Methods

### Cells

The murine 005 mGSCs were established from a GBM generated by lentiviral transduction of Harvey-Ras$^{V}$12 (H-Ras) in a GFAP-cre, Tp53$^{+/-}$ transgenic mouse.[21] They were provided by Dr. I. Verma (Salk Institute). NF53-10 mGSCs were derived by transduction of GFAP-cre neural stem cells with lentivirus expressing shRNAs targeting Nf1, Tp53, and Pten.[23,33] RIG-C1, C1, and C3-1 mGSCs were established from GBMs induced by lentivirus expressing H-Ras$^{V}$12 and shRNA for Tp53.[34] NF53-10 and RIG-C1 mGSCs were provided by Y.S., and C1 and C3-1 by T.H., and were established in the Verma lab. All these mGSC lines are GFP-positive. Hereafter, we simplify the names for the mGSCs; C3-1 as C3, RIG-C1 as RIG, and NF53-10 as

NF53. CT2A cells were provided by Dr. T. Seyfried (Boston College).[17]

The 5 mGSC lines were cultured as nonadherent spheres in serum-free stem cell media, composed of advanced Dulbecco's modified Eagle's medium/Ham's F-12 (DMEM/F-12) (Thermo Fisher Scientific), supplemented with L-glutamine (2 mM; Corning), 1% N2 supplement (Thermo Fisher Scientific), 2 µg/mL heparin (Sigma), 20 ng/mL recombinant human EGF (R & D Systems), and 10 ng/mL recombinant human FGF (Peprotech). Cells were passaged after dissociating neurospheres with Accutase (Innovative Cell Technologies) and maintained at 37°C in humidified atmosphere air: $CO_2$ (95%:5%).

## Whole Exome Sequencing

Whole exome sequencing (WES) was performed by Novogene on DNA purified from the 5 mGSCs and CT2A cells. Libraries were constructed from randomly sheared genomic DNA, PCR amplified, exons captured, and Illumina sequenced. Burrows-Wheeler Aligner was used to map the reads to the mouse reference genome (mm10). Coding region single nucleotide polymorphisms (SNPs) or variants (SNVs) were identified by comparison with the C57BL/6J genome reference sequence (GRCm38) (Figure 1B).

## Self-Renewal Sphere Formation Assay

Cells dissociated with Accutase were passed through a 40-µm filter to produce single-cell suspensions, with viable cells counted after trypan blue staining, resuspended in stem cell media, and seeded into 96-well plates at the indicated number of cells per well. Eight to twelve days later, the number of spheres (diameter > 100 µm) and wells containing spheres were counted. Sphere efficiency was evaluated with extreme limiting dilution analysis.[22]

## In Vivo Experiments

Dissociated mGSCs ($2 \times 10^4$ or $1 \times 10^5$ cells suspended in 2 µL of DMEM) were stereotactically implanted intracerebrally in the right striatum (2.5 mm lateral from bregma and 2.5 mm deep) of 8- to 9-week-old female C57Bl/6 mice (Jackson Laboratory) under pentobarbital anesthesia using a stereotactic head frame (Kopf). For survival studies, mice were monitored at least 3 times a week for significant neurological symptoms (such as hemiparesis or lethargy) or weight loss exceeding 20% and euthanized by barbiturate overdose before becoming moribund. All mouse procedures were approved by the institutional animal care and use committee at Massachusetts General Hospital.

## Immunohistochemistry

Immunohistochemistry was performed similarly as described in.[35] Rehydrated sections (as in Histochemistry [Supplementary Material]) were washed with PBS twice, and antigen retrieval performed by heating in a microwave in 10 mM sodium citrate buffer (pH = 6.0) for 15 minutes, cooled, washed with PBS twice, and incubated with 3% $H_2O_2$ (5 minutes) to block endogenous peroxidase activity. Following washing twice with PBS, sections were incubated with 2.5% normal horse or goat serum (Vector Laboratories) for 40 minutes for blocking. Then, sections were incubated with indicated primary antibodies (Supplementary Table S1) overnight at 4°C, washed in PBS 3 times, and incubated with ImmPRESS HRP anti-rabbit, -mouse, or -rat IgG polymers (Vector Laboratories) for 30 minutes at room temperature (RT). After washing with PBS 3 times, staining was developed with DAB (Vector Laboratories), counterstained with hematoxylin, and treated as in Histochemistry. For immunofluorescent staining, Anti-fade DAPI solution (Vector Laboratories) was applied, and sections cover-glass mounted.

## Flow Cytometry

In vitro CD133, MHC-I, and MHC-II expression on Accutase-dissociated mGSCs was determined by flow cytometry. Cells were stained with phycoerythrin (PE)-conjugated anti-CD133, or anti-MHC-1 (H-2Kb)-PE, or anti-MHC class II (I-AE)-BV650 (Supplementary Table S1) for 30 minutes, washed and fixed in 2% paraformaldehyde, run on a BD LSR II flow cytometer, and data analyzed by FlowJo software.

For fluorescence-activated cell sorting (FACS) analysis of tumor-infiltrating immune cells (as described in[36]), brain tumor tissue was harvested when tumor-bearing mice began to show weight loss, and single-cell suspensions were prepared by 10-minute digestion of minced tumor tissue in 1 mL of Accutase containing 10 U/mL DNase I (Sigma) at 37°C. Tumor digestion was stopped by adding Advance-DMEM/F-12 containing 10% fetal bovine serum (Invitrogen), and the suspension was filtered through a 70-µm mesh and washed twice with PBS. Before surface staining, the samples were preincubated with anti-CD16/32 unconjugated antibodies (clone 93) to block Fc receptor binding. Samples were subjected to surface staining with fluorochrome-conjugated antibodies. Samples were stained with ef450 fixable viability dye to discriminate dead cells. To detect Foxp3+ Tregs, samples were stained intracellularly using FoxP3 fix/perm buffer set (BioLegend, Cat. # 421403). Antibody details are listed in Supplementary Table S1. Samples were run on a BD LSR II or FACS Aria flow cytometer, with FlowJo version (v.)10 software (Tree Star) used for data analysis.

## Statistical Analysis

Survival data were plotted as Kaplan–Meier survival curves. To compare the Ki67 index between core and edge, an unpaired Student's *t* test (2-tailed) was used. For the statistical analysis of immunohistochemistry and FACS comparing the 5 mGSC models, 1-way ANOVA with Tukey's multiple comparisons test was used. The number of replicates for FACS analysis ranged from $n = 3$ to $n = 7$ mice per group. Error bars represent the mean ± SD. Statistical significance was set at $P < 0.05$. All statistical computations were conducted using GraphPad Prism software version 10.0.2.

## Results

### mGSC Models Driven by Alterations of the Ras and Tp53 Signaling Pathways

Five mGSC lines driven by NF1-Ras-MAPK signaling activation and Tp53 inactivation were established from tumors arising after lentivirus transduction of discrete regions of the brain or neural stem cells of genetically engineered mice (Figure 1A). WES was performed to quantify the number of SNPs, using the genome of the inbred C57BL/6J strain as the reference. Here we noted a large variation in the number of SNPs in the genome-wide coding sequences (Figure 1B). 005 has the highest number of non-synonymous SNPs (7405), roughly double those of RIG (4100) and NF53 (4020), which were derived with different oncogenes/tumor suppressors. In contrast, C1 and C3 had the lowest SNP counts, only 508 and 533, respectively (Supplementary Table S2). This variation is also reflected in the InDel numbers (Supplementary Table S2). Much of this difference in SNP counts is likely due to the variable mixed background of the GFAP-cre/Tp53 transgenic mice used for deriving different mGSCs. The variability can be compared to CT2A (3539), a commonly used syngeneic GBM model, which was derived from a chemical carcinogen-treated C57BL/6 mouse.[17] Thus, the 5 mGSC models have variable and distinct SNP counts, as well as InDels, despite being generated using a similar genetic engineering approach. They are an important addition to the limited number of murine GBM cell lines and provide useful models to evaluate the role of tumor mutational burden on immunotherapy. We next set out to examine stem cell features, tumorigenicity, and the TME to comprehensively characterize our GSC models (Figure 1C).

### In Vitro Stem Cell Features of mGSCs

GSCs have been characterized by their growth as nonadherent spheres in serum-free media containing EGF and FGF, efficient and lethal tumorigenicity, and differentiation into more mature cells.[37,38] We characterized the 5 mGSC lines for their stem cell-like properties by analysis of sphere formation, expression of stemness markers such as CD133, Sox2, Olig2, and Nestin,[39] and differentiation. Limiting dilution assays confirmed that all of the mGSCs were capable of sphere formation with varying efficiencies or frequencies of sphere formation (Figure 1D and E). RIG and C1 showed the most efficient sphere formation with 1/13 and 1/7 stem cell frequencies, respectively. Flow cytometric evaluation of cell surface expression of CD133, a putative, but controversial brain tumor stem-like cell marker,[40–42] on dissociated cells, revealed varying levels of CD133; 45%, 62%, and 23% of CD133+ cells on 005, RIG, and C3 mGSCs, respectively, while negligible on NF53 and C1 cells (Figure 1F).[43] Immunocytochemistry for GSC markers showed varied expression of Olig2 (nuclear) between mGSCs with high levels in C3, and consistent strong expression of Sox2 (nuclear) and nestin (cytoplasmic) across mGSCs (Supplementary Figure S1). Serum-induced differentiation of mGSCs resulted in morphological changes characterized by cell body enlargement and elongated process formation (Supplementary Figure S2A), and expression of neuronal markers βIII tubulin and MAP2 (Supplementary Figure S2B and C) and astrocytic marker GFAP (Supplementary Figure S2D). Since temozolomide (TMZ) is a part of the current standard of care for GBM, we evaluated the cytotoxic effects of TMZ on mGSCs in vitro. 005 GSCs showed moderate sensitivity to TMZ, as was previously reported,[44] otherwise, the other 4 mGSCs were somewhat resistant to TMZ (Supplementary Figure S3). Taken together, these data show that the 5 mGSC lines are all capable of sphere formation and multi-lineage differentiation, cardinal in vitro features of GSCs.

### In Vivo Tumorigenicity

To evaluate mGSC tumorigenicity in immunocompetent mice, 2 doses ($2 \times 10^4$ or $1 \times 10^5$ cells) of cells were implanted intracerebrally into the right striatum of C57Bl/6 mice. MGSCs consistently formed lethal tumors, regardless of the implanted cell number, with the median survival times following implantation of $1 \times 10^5$ cells ranging from 22 days (NF53) to 70.5 days (C1) (Figure 2A). At the terminal stage, tumors were typically visible macroscopically on the surface of the brain at the site of implantation (Figure 2B). Hematoxylin and eosin staining of paraffin-embedded sections revealed massive tumors for all mGSCs, typically occupying the implanted right hemisphere, displacing the surrounding and midline brain structures (Figure 2C). Histologically, all the tumors were densely cellular and composed of primitive-looking neoplastic cells. 005, RIG, and C1 exhibited rather well-defined margins, with focal brain invasion, while NF53 showed diffuse infiltration into the adjacent brain and along blood vessels (Virchow Robin spaces), recapitulating human tumors (Figure 2C; Supplementary Table S3). C3, in contrast, had sharp borders, with focal infiltration to the adjacent brain (Figure 2C; Supplementary Table S3). Mitotic figures were frequent in all tumors, indicative of active proliferation (Figure 2D). Thus, upon orthotopic implantation in immunocompetent mice, mGSCs reproducibly generate malignant tumors characteristic of human GBM (Supplementary Table S3).

### Invasiveness and Proliferation Phenotypes of mGSC-Derived Tumors

Since the mGSCs express GFP, staining with anti-GFP antibody was used to clearly reveal the infiltrative nature of the tumors (Figure 3A; Supplementary Figure S4A). NF53 exhibited a particularly invasive phenotype as neoplastic cells migrated along the corpus callosum and extended to the contralateral hemisphere. 005 and C1 tumors reached the midline. RIG tumors had numerous foci migrating away from the main tumor mass (Figure 3A). Conversely, despite the large size, C3 tumors were confined to the implanted hemisphere (Figure 3A). On examination with higher magnification there was evidence for microscopic invasion in all the models (Supplementary Figure S4A). Characterization of tumor proliferation using Ki67 immunohistochemistry revealed variable but overall high Ki67 indices ranging from 20% to 43%, consistent with

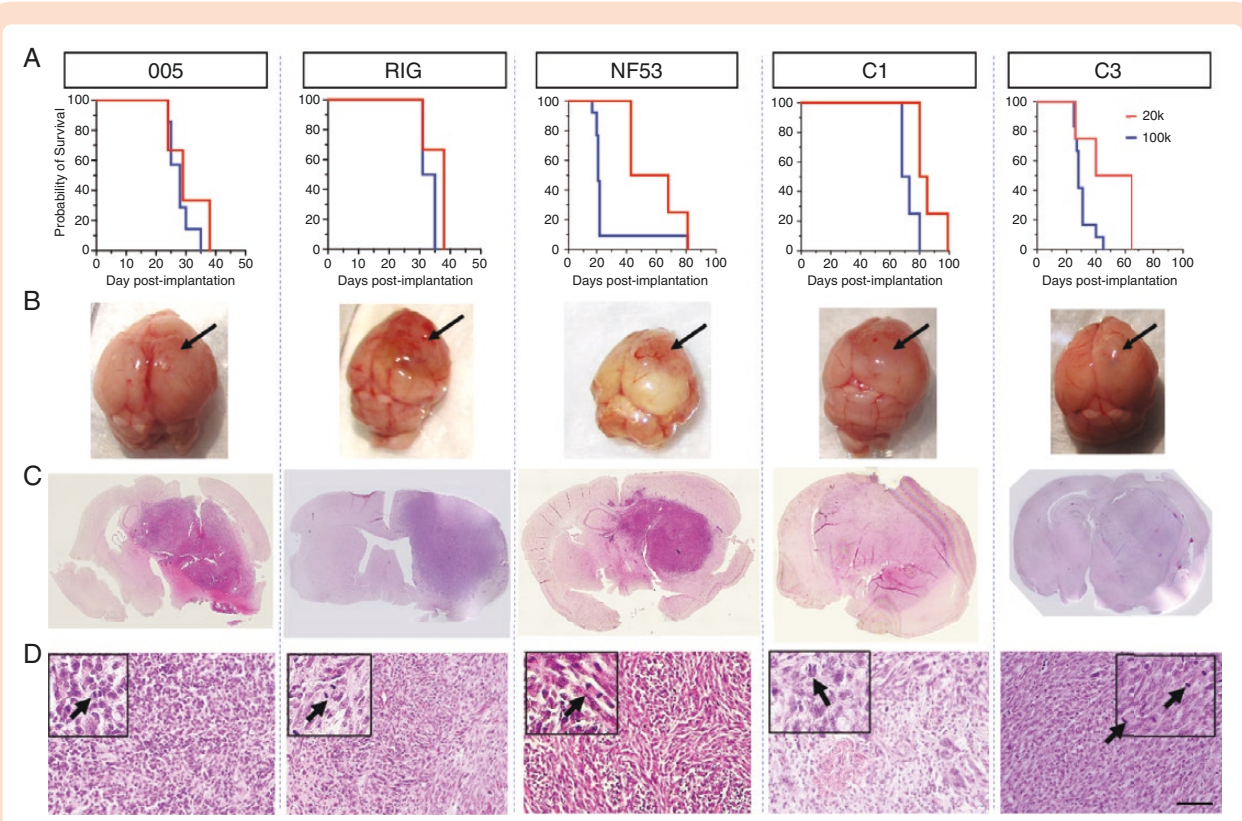


**Figure 2.** In vivo tumorigenicity and histopathology of murine glioblastoma stem-like cell (mGSC)-derived tumors in C57BL/6 mice. (A) Kaplan–Meier survival curves of C57Bl/6 mice implanted intracerebrally with $2 \times 10^4$ (20k, red [line to right]; $n = 4$ mice per group except $n = 3$ for 005 and RIG) or $1 \times 10^5$ (100k, blue [line to left]; $n = 4$ for RIG and C1, $n = 11$ for 005, and $n = 12$ for NF53 and C3) mGSCs/mouse. (B) Brains from C57BL/6 mice with advanced-stage tumors. Arrows indicate the implantation sites. (C) Hematoxylin and eosin (H&E)-stained coronal sections of mouse tumor-bearing brains. Low-magnification images were patched together. (D) Higher magnification of H&E-stained tumor sections. Arrows in 20× magnification insets indicate mitosis. Scale bar = 50 μm.

the malignant phenotype of the tumors (Figure 3B and C). Image analysis of Ki67-stained slides suggested that density of Ki67 immunopositivity was heterogeneous within the tumor mass (Supplementary Figure S4B). We therefore compared the Ki67 proliferation index between the edge and core of the tumors, by quantifying the Ki67-positivity in 3 fields from the tumor edge and 3 from the tumor core. C1 and C3 tumors showed a tendency toward a higher Ki67 index in the edge areas, but without statistical significance (Figure 3D).

## Stemness, Differentiation, and Heterogeneity of mGSC Tumors In Vivo

We next performed immunohistochemical staining of several GSC markers in vivo. Nuclear Sox2 was highly expressed in all the models, except 005, exhibiting modest expression, and C1 with positivity in a small subset of cells (Figure 4A). All the mGSC tumors showed intense immunopositivity for Nestin, except for NF53 (Figure 4B). Neoplastic expression of Nestin was confirmed by co-immunofluorescence of Nestin and GFP (Supplementary Figure S5A). Proneural and oligodendroprogenitor cell (OPC) marker Olig2, was nearly negative in RIG, focally positive in NF53, C1, and C3, and positive in 005 tumors (Figure 4C). The stem and mesenchymal marker CD44, on the other hand, was diffusely positive in all 5 mGSC tumor models (Figure 4D), and its cytoplasmic and membranous expression delineated tumor–brain border regions (Supplementary Figure S5B). Double immunofluorescence of Olig2 and CD44 confirmed consistently high expression of CD44 in our models (Supplementary Figure S6). Olig2+ cells were prevalent in 005, but patchy or scattered in the other mGSC tumors (Supplementary Figure S6). Olig2+ cells were typically double-positive for CD44, but foci of Olig2+/CD44– tumor cells, distinct from Olig2–/CD44+ areas, were noted in C3 tumors (Supplementary Figure S6), suggesting divergent lineage differentiations. In addition, immunohistochemistry for GFAP, an astrocytic marker, revealed that a significant proportion of tumor cells were GFAP-positive in all 5 mGSC tumors (Figure 4E). β-III tubulin staining revealed high positivity in 005 and C3 tumors, and low expression in RIG tumors (Figure 4F). RNA sequencing analysis of the mGSC tumors showed expression patterns for these stemness genes that were generally concordant with immunohistochemistry and immunofluorescence results (Figure 4G), as Olig2 expression varied greatly among the models. Gfap mRNA expression was variable (Figure 4G) and did not correlate with GFAP

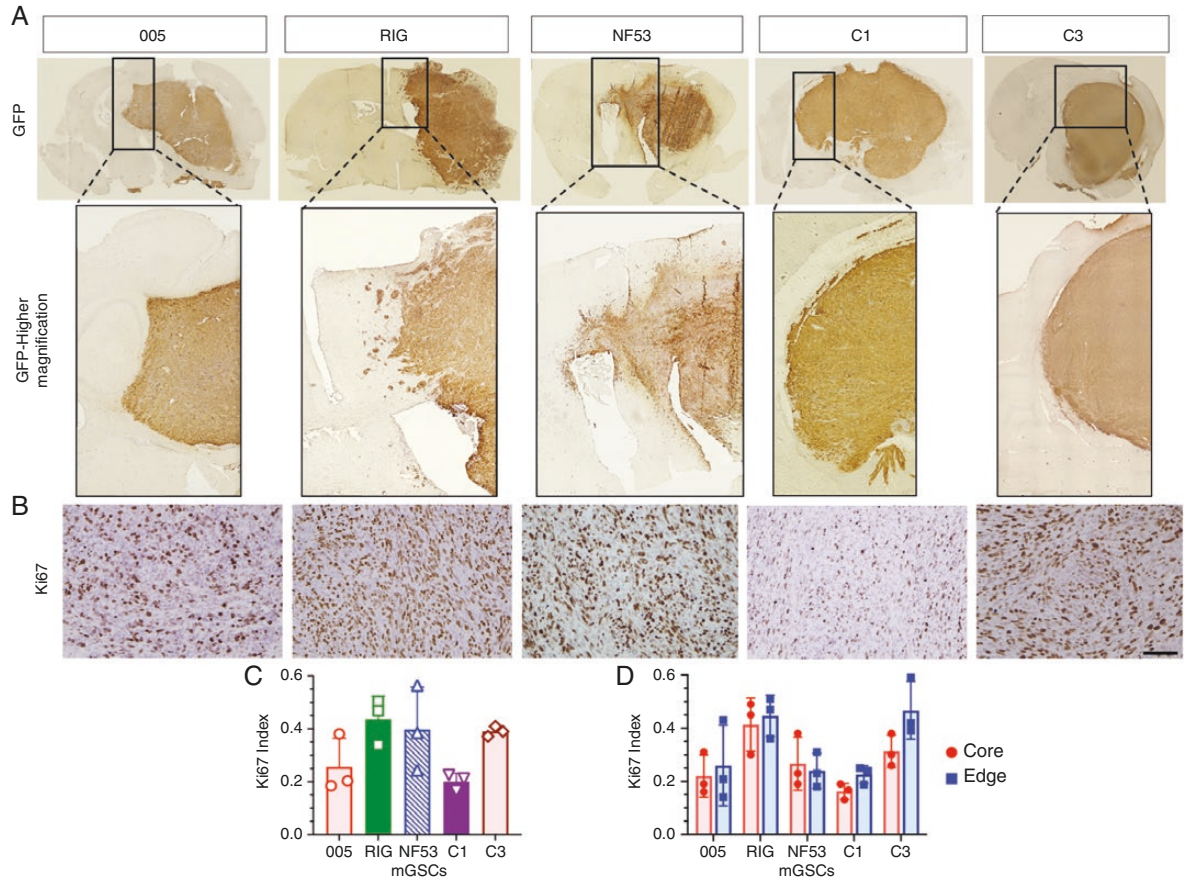


**Figure 3.** Tumor cell infiltration and proliferation in murine glioblastoma stem-like cell (mGSC)-derived tumors. (A) Upper. Coronal sections of mouse advanced-stage tumor-bearing brains after anti-GFP immunohistochemistry (brown [dark stain]; tumor cells). 10× magnification images were patched together. Same brains as in Figure 2. Lower. Magnification of GFP staining from the rectangles in top panels showing the tumor–brain interface and tumor invasiveness at or near the corpus callosum, with NF53 crossing to the contralateral hemisphere. (B) Representative images of immunohistochemical staining of proliferation marker Ki67 (brown [dark] nuclei), with hematoxylin counterstaining. Scale bar = 50 µm. (C) Quantification of Ki67 positive cells (Ki67 index) from 6 fields/tumor section/mouse from 3 mice (individual symbols). No statistical difference was noted (1-way ANOVA with Tukey's multiple comparisons test). (D) Ki67 indices comparing tumor core and edge (periphery) regions in each model. Mean ± SD is plotted. No statistical difference was noted in any tumor models (unpaired Student's *t* test, 2-tailed).

immunohistochemistry (Figure 4E). Thus, although consistently expressing mesenchymal CD44, our models also exhibit proneural and OPC phenotypes, evidence for phenotypic heterogeneity, a hallmark of human GBM. These data also show the capacity of the mGSC tumors for multilineage differentiation in vivo.

To determine whether our mGSC tumors recapitulate the cellular state heterogeneity characteristic of human GBM, we analyzed our RNA sequencing data to identify the distinct cellular states defined by Neftel et al. in human GBM cells.[45] Similar to what was reported with murine GBM models created with lentiviruses harboring H-Ras and shP53,[45] we noted the presence of the MES1-like, MES2-like, as well as the OPC-like states in most of our models (005, NF53, and C1), while the AC-like state was nearly absent (Supplementary Figure S7). Comparative analysis using 8 human GBMs (GSE266210) demonstrated similar patterns of cellular state distributions, as these patient tumors are composed of dominant MES1- and MES2-like cells and variable and lower frequencies of OPC-like and AC-like cells (Supplementary Figure S7).

## Characterization of Tumor-Infiltrating Immune Cells

A critical hallmark of human GBM is its highly suppressive TME characterized by dominant myeloid cells, such as tumor-associated macrophages (TAMs), and less T-cell infiltration.[46] Immunohistochemistry was first used to evaluate the infiltrates of immune cells in the TME of the mGSC tumors in the brain at their terminal stage. There was a notable variation in the level of tumor-infiltrating lymphocytes (TILs) between mGSC-derived GBMs. The NF53 tumors contained the highest levels of infiltrating of CD3+, CD4+, and CD8+ T cells, with NF53 significantly higher than C1 and C3 (Supplementary Figure S8A–C). C1 and C3 GBM models demonstrated the lowest quantity of TILs (Supplementary Figure S8A–C). Tumor-infiltrating

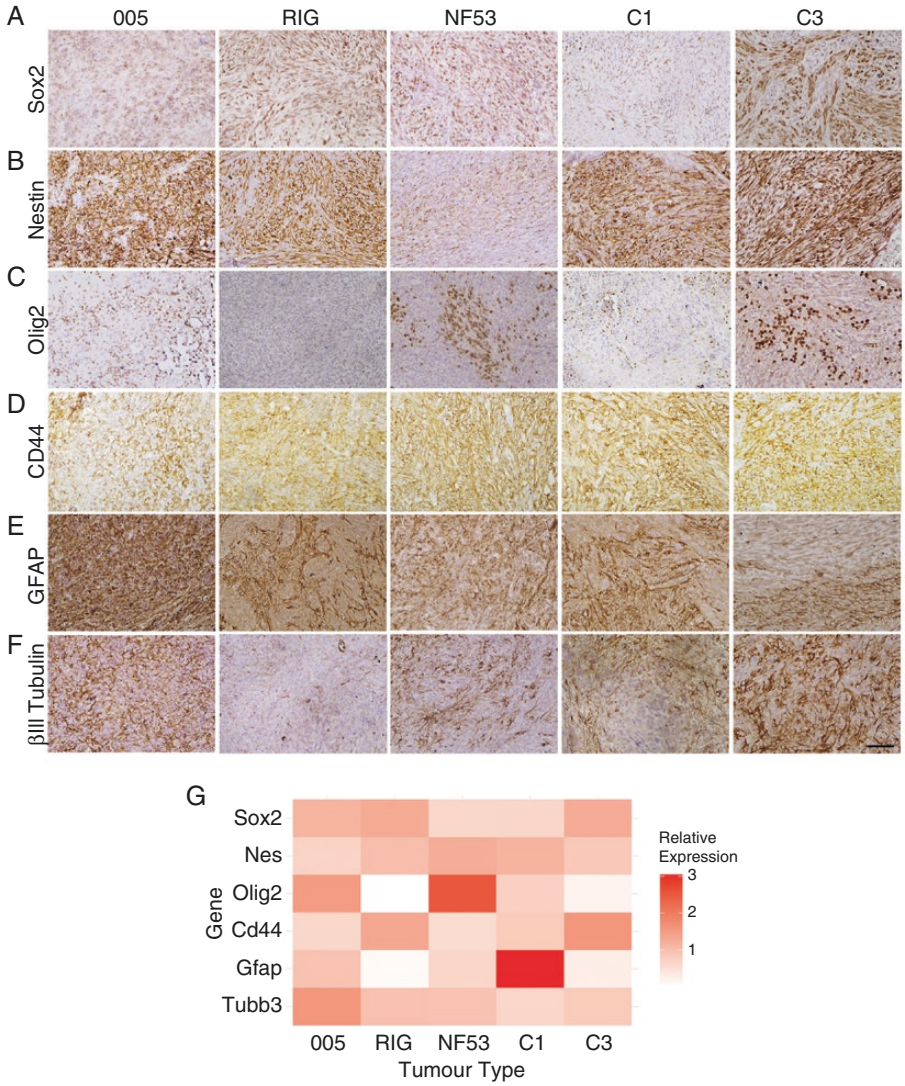


**Figure 4.** Immunohistochemical characterization of stemness and differentiation markers in murine glioblastoma stem-like cell (mGSC)-derived tumors. Sections (7 μm) from mouse brains with advanced-stage tumors were stained for stemness markers; (A) Sox2, (B) Nestin, (C) Olig2, (D) CD44, and differentiation markers; (E) GFAP, and (F) βIII tubulin. Representative images with positive cells stained brown (dark). Scale bar = 50 μm. (G) Relative FPKM values of RNA sequencing of whole tumors. FPKM values were divided by the mean of all 5 tumors for each gene.

macrophages, marked by CD68-positive cells, were generally abundant without a large variation between mGSCs (Supplementary Figure S8D), consistent with the dominant presence of macrophages in the GBM TME. Arg1 that has been commonly used to mark immune suppressive macrophages[47,48] was generally prevalent in the GSC tumors (Supplementary Figure S9). Immune checkpoint ligand PD-L1 is a major contributor of immune suppression in the TME of cancer, including GBM. PD-L1-positive cells were readily detectable by FACS in the TME of all the mGSC GBM models, with especially high proportions of positive myeloid cells in all mGSC tumors, and on RIG and C1 cells (Figure 5D). Its expression levels by IHC were not notably different between the mGSCs (Supplementary Figure S8E).

One intrinsic feature of GBM escape from immune surveillance is the downregulation of MHC expression to evade T-cell killing.[49,50] Among the mGSCs, only RIG expressed significant levels of MHC-I ($P < 0.0001$ 1-way ANOVA with Tukey's multiple comparisons), with minimal expression in the other mGSCs (mean < 3.1%), while MHC-II expression was negligible in all mGSCs (mean < 2.5%; Supplementary Figure S10).

## Flow Cytometric Profiling of Tumor-Infiltrating Immune Cells

To provide a comprehensive analysis of the immune cell composition in our 5 mGSC-derived GBMs, we performed a multi-parametric flow cytometry analysis of the right frontal brain quadrant containing advanced-stage tumors. Viable cells isolated from the TME were initially analyzed for

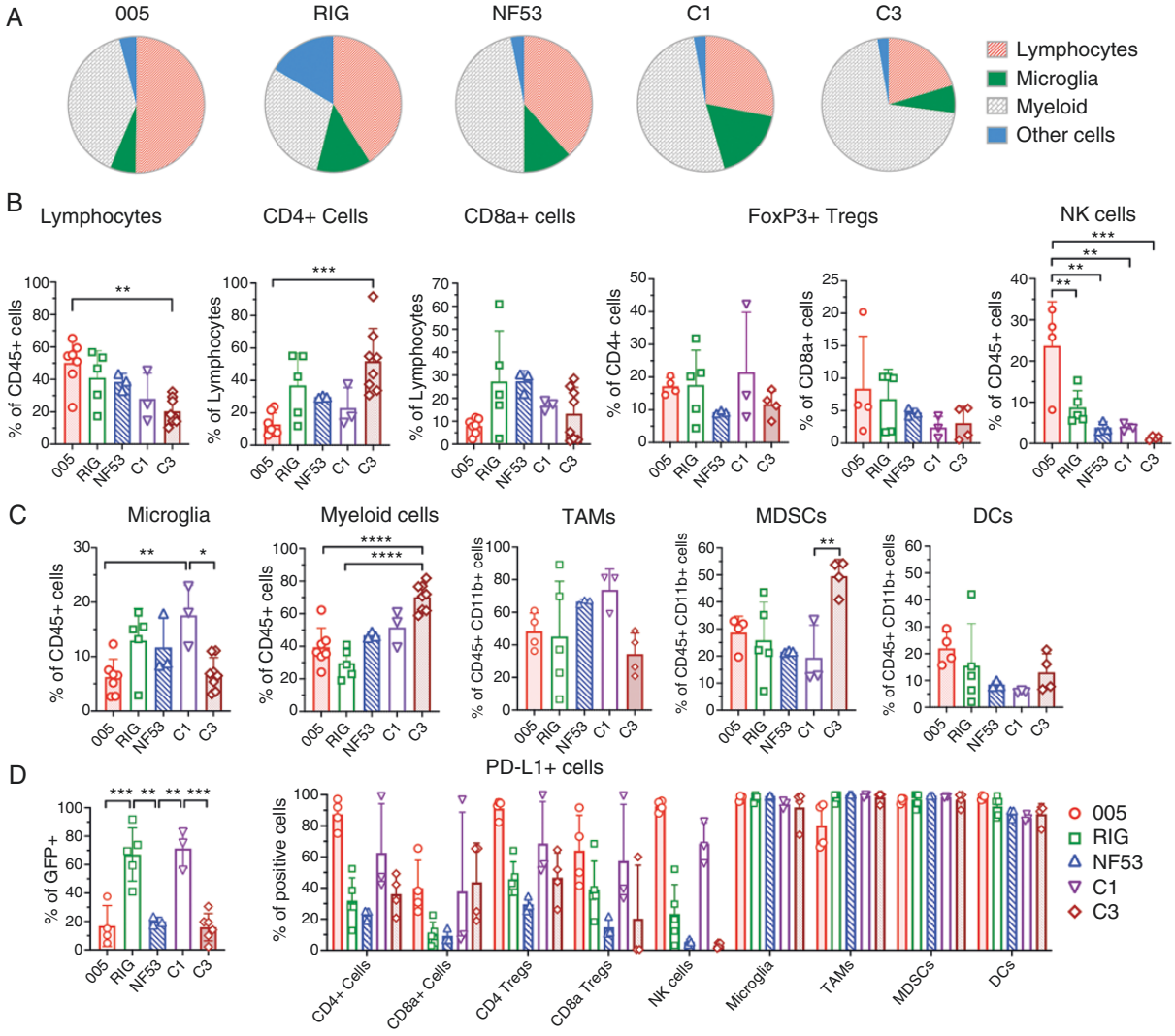


**Figure 5.** Fluorescence-activated cell sorting (FACS) analysis of immune cell subsets in murine glioblastoma stem-like cell (mGSC)-derived tumors. Following intracerebral implantation of 005, RIG, NF53, C1, and C3 mGSCs ($1 \times 10^5$), advanced-stage tumors were subjected to FACS analysis ($n = 3$–7 mice per group). Gating scheme is shown in Supplementary Figure S8. (A) Pie charts show the relative proportion of immune cell subsets within the total CD45+ cell population: myeloid cells (CD45$^{high}$/CD11b+), microglia (CD45$^{low}$/CD11b+), lymphocytes including both B and T cells (CD45$^{high}$/CD11b–), and other cells (CD45$^{low}$/CD11b–) in mGSC-derived tumors. (B–D) Histograms displaying the relative abundance (percentage) of specific immune cell populations from FACS. (B) Lymphocyte subtypes. Fractions of CD4+ T cells and CD8a+ T cells within lymphocytes, regulatory T cells (Tregs) within CD4+ and CD8a+ T cells, and natural killer (NK) cells within CD45+ cells. (C) Microglia (CD45$^{low}$/CD11b+) and myeloid cells (CD45$^{high}$/CD11b+). Myeloid cells were classified into tumor-associated macrophages (TAMs) (F4/80$^{high}$), myeloid-derived suppressor cells (MDSCs) (F4/80$^{mid}$), and dendritic cells (DCs) (F4/80–). (D) PD-L1+ cells within GFP+ tumor cells (left) and different immune cell types (right). Error bars represent the mean ± SD. Statistical analyses were conducted using 1-way ANOVA with Tukey's multiple comparisons test. *$P < 0.05$; **$P < 0.01$; ***$P < 0.001$; and ****$P < 0.0001$.

GFP to assess tumor burden (Supplementary Figures S11 and S12A). Subsequently, viable cells were separated into CD45– and CD45+ subsets (Supplementary Figures S11 and S12B). CD45+ cells were gated into CD45$^{high}$/CD11b– cells, CD45$^{high}$/CD11b+, and CD45$^{low}$ cells, followed by further phenotyping (Supplementary Figure S11). Immune cell composition varied substantively across the 5 models. In 005 and RIG tumors, lymphocytes were the dominant immune cell subset representing 40%–50% of the total CD45+ cells (Figure 5A), conversely, myeloid cells were the dominant subtype in NF53, C1, and C3 tumors (Figure 5A and C). C1 and C3 tumors had the lowest fraction of lymphocytes, occupying only 28% and 20% of CD45+ cells (Figure 5A and B). The CD4+/CD8+ ratio was close to 1, except for C3 with a skewed high CD4+/CD8+ ratio (Figure 5B). FoxP3+ regulatory T cells (Treg) represented 18%–35% of CD4+ T cells and only 2%–8% of CD8+ T cells across all mGSCs (Figure 5B). NK1.1+ NK cells were a minor subset within CD45+ cells, except in 005 tumors with a predominant NK population within the lymphoid subset (Figure 5B).

**Table 1.** Summary of Key Features of the mGSC Models

| GSCs | 005 | RIG | NF53 | C1 | C3 |
|---|---|---|---|---|---|
| Genetic drivers | $HRas^{v12}$, $Tp53^{-}$ | $HRas^{v12}$, Tp53 shRNA | Nf1 shRNA, Tp53 shRNA, Pten shRNA | $HRas^{v12}$, Tp53 $shRNA^{-}$ | $HRas^{v12}$, p53 shRNA |
| Mutation load | High | Mid | Mid | Low | Low |
| Clonogenicity (%)[a] | Low (2.5) | Mid (7.0) | Mid (4.1) | High (12.8) | Low (2.7) |
| CD133 (%) | Mid (45) | High (62) | Low (0.03) | Low (0.01) | Mid (23) |
| Survival (days)[b] | 28/29 | 33/38 | 20/55 | 71/82 | 28/53 |
| Ki67 (%) | 26 | 43 | 39 | 20 | 39 |
| Invasiveness | + | ++ | +++ | + | – |
| Sox2 | + | ++ | ++ | + | ++ |
| Nestin | ++ | ++ | + | ++ | ++ |
| Olig2 | + | – | ++ | + | ++ |
| CD44 | ++ | +++ | +++ | +++ | +++ |
| Immune profile | Lymphocytes dominant[c] | Relative lymphocytes dominant | CD8+ T cells and TAM dominant | TAM/microglia dominant T cells depleted | MDSC dominant T cells depleted |

**Abbreviations:** MDSC, myeloid-derived suppressor cells; mGSC, murine glioblastoma stem-like cell; TAM, tumor-associated macrophages.
[a]% sphere-forming cells.
[b]Median survival time post-implantation of 100 000 cells (left) and 20 000 cells (right).
[c]Including T, B, and NK cells.

Microglia ($CD11b+/CD45^{low}$) occupied 6%–18% of CD45+ cells in the TME (Figure 5A and C). Interestingly, the fraction of microglia differed greatly in the 2 TIL-low models, C1 (18%) and C3 (7%) (Figure 5A and C). The CD45+CD11b+ myeloid populations were further gated into TAMs ($F4/80^{high}$), myeloid-derived suppressor cells (MDSCs) ($F4/80^{mid}$) and DCs (F4/80–) (Supplementary Figure S11). TAMs consistently represented a major fraction of myeloid populations (>30%) in all the models (Figure 5C), recapitulating the TAM-dominant TME of human GBM.[46] The degree of MDSCs infiltration varied, with C3 having the largest fraction (49%) within the myeloid population (Figure 5C). DCs were a minor myeloid subset consistently across the 5 models (Figure 5C). Of note, the TME of C1 was characterized by the highest fraction of microglia and TAMs and the lowest fraction of MDSCs, while C3 TME had the opposite distribution (Figure 5C). Neoplastic expression of PD-L1 was variable, with RIG and C1 frequently (>60%) containing PD-L1+ GBM cells (GFP+; Figure 5D). Furthermore, a variety of immune cells expressed PD-L1, most notably microglia and myeloid cell populations exhibiting very high proportions (>80%) in all the mGSC models, while lymphocytes and NK cells in 005, and less so in C1 tumors were also very high (mostly >50%; Figure 5D). As expected, only a very small fraction of neoplastic cells expressed PD-1 (Supplementary Figure S12C). Average TIL PD-1 expression ranged from 10% to 32% and varied between the models and among animals (Supplementary Figure S12D). Based on transcriptional T-cell markers described in Wang et al.,[51] we also showed that the pattern of T-cell activation, cytotoxicity, and exhaustion was similar to that of human GBM tumors, with upregulation of most markers in these 3 categories (Supplementary Figure S13). We assessed potential correlations between tumor burden (GFP+) and immune cell subsets (Supplementary Figure S14). Although we did not observe any consistent trends across the models, larger NF53 tumors were associated with lower immune cell (CD45+) infiltration driven by a decline in microglia. On the other hand, the C1 tumor burden positively correlated with microglia and myeloid populations while negatively correlated with the lymphoid population ($R^2 \geq 0.6$; Supplementary Figure S14). To understand whether our mGSC models have the immune TMEs that mirror the human GBM TME, we analyzed the flow cytometry data from 6 human GBM biopsy specimens that utilized a gating strategy similar to ours.[52] CD45+ immune cells were a major component of human GBMs and were dominated by CD11b+ myeloid populations (including macrophages and MDSCs), with typically a smaller contribution of lymphocytes (Supplementary Figure S15). This immune profile was similar to what was observed in the immune TMEs of our mGSC models (Figure 5). Collectively, flow cytometric profiling of our mGSC-derived GBMs revealed a generally suppressive, but distinct immune landscape of the TME for each model. In Table 1, we summarize key genomic and phenotypic features of our 5 mGSC models.

## Discussion

The scarcity and limited characterization of immunocompetent GBM models representative of human GBM hinder the development of effective therapeutic strategies for GBM. Here, we characterized 5 mGSC lines driven by activation of the NF1-Ras MAP kinase signaling pathway and inactivation of the tumor suppressor Tp53. Despite similar genetic alteration strategies being used to establish these models, we found an unexpected and remarkable diversity between the models in essentially every feature

we investigated relevant to GBM and GSC biology, for example, stem-like properties in vitro and in vivo and the immune microenvironment (Table 1).

WES revealed a large variability in the number of SNPs among the 5 mGSC lines, and compared to CT2A. We speculate that variation in the mixed genetic backgrounds of the Tp53$^{-/+}$, GFAP-Cre mice used for generating the mGSCs was a major contributor to SNP differences. 005 mGSCs, which have been used extensively in recent years for immunotherapy and other research applications,[11,20,23–28] had the highest number of SNPs. However, despite the high number of SNPs, and likely associated neo-antigens and allogeneic character, 005, as well as RIG and NF53 mGSCs, efficiently formed consistently lethal tumors in C57BL/6 mice, providing reliable immunocompetent GBM models. Checkpoint immunotherapy was only modestly effective in the 005 model,[24,26,27] as opposed to its reproducible significant activity against the commonly used, chemically induced GL261 GBM model.[53] Interestingly, the reported non-synonymous SNP number in GL261 was about 5000,[18,53] lower than that found in 005. C1 and C3 mGSCs, on the other hand, had by far the fewest SNPs (10– to 20-fold less), likely reflecting the near-pure C57BL/6 background of the mice used. Recently, Chen and colleagues reported a series of murine GBM models driven by deletion of Qki, and Tp53 and Pten tumor suppressors, termed QPPs.[54] WES of the QPP GBMs showed a range of SNP counts when the C57BL/6 genome was used as the reference. The SNP counts found in 3 of the 4 QPP models were comparable to those we observed in 005 mGSCs, the highest among our mGSC models, highlighting the lower mutation burden in most of our models, particularly C1 and C3. The only GBM model syngeneic to C57BL/6 mice that was reported to have a lower SNP level than C1 and C3 is SB28, which was generated by sleeping beauty transposon-mediated transduction of NRasV12, shTp53, and mPDGF[55] and was nonresponsive to checkpoint immunotherapy.[53] Mut3 and KR158 represent transplantable GBM models that were derived from malignant gliomas spontaneously arising in genetically engineered mice harboring Nf1 and Tp53 mutations.[56,57] The KR158 model in C57BL/6 mice has been utilized for some immunotherapy research, including direct comparisons with 005 and GL261.[58–60] None of these mouse GBM cell lines were isolated as mGSCs. Our panel of mGSCs, thus, furnish new useful models to evaluate the role of tumor mutation burden on GBM immunotherapy.

Our assessment of stem-like features demonstrated that all mGSC lines exhibited sphere-forming capabilities at low cell numbers, a hallmark of stem cell behavior. Additionally, these cells expressed markers commonly associated with neural stem/progenitor cells and exhibited differentiation potential. However, we observed differences in their stem-like characteristics. Notably, CD133 expression, one of the more commonly described GSC markers,[61] varied greatly among the mGSC lines, from negligible to 62%. We did not find a positive correlation between CD133 levels and sphere formation as C1 and C3 mGSCs having no detectable or 23% CD133 expression had the highest and lowest efficiency, respectively, of clonogenicity in vitro. All the mGSCs were reliably tumorigenic in vivo upon orthotopic implantation of 20 000 cells. C1 mGSCs displayed the most efficient sphere formation but was the least aggressive in vivo, with the longest mouse survival. NF53 with no CD133 expression had the shortest median survival time with 100 000 cells implanted. CD133 has been often suggested as one of the defining characteristics of GSCs and has even been linked to self-renewal and tumorigenicity.[41,61–63] However, our finding of an apparent discordance between CD133 levels, clonogenicity, and animal survival suggests a context-dependent role of CD133 in mGSC biology and that no single parameter correlates with in vivo tumorigenicity.

In vivo characterization of the mGSC-derived tumors revealed variable aggressiveness and histopathological features. The highly infiltrative nature of NF53 tumors along the corpus callosum is of particular interest, as it mirrors a common growth pattern observed in humans. These variations in tumor phenotypes provide valuable platforms for investigating mechanisms underlying tumor invasion and potential therapeutic targets. Regarding stem/progenitor markers in vivo, there was variability in the level and distribution of expression of Sox2, sparser in 005, C1, and nestin, and sparse in NF53. Mesenchymal CD44 was generally diffuse, while proneural/OPC marker Olig2-expressing cells were heterogeneously distributed. This illustrates the heterogeneity in phenotypes or cell states, and the likely plasticity of the mGSCs (Table 1; Figure 4; Supplementary Figure S6 and S7). This observation is in line with what was described in Neftel et al.,[45] where murine GBM generated with a lentivirus harboring HRasV12 and shTrp53, genetic drivers identical to our models, exhibited multiple cellular states, including astrocytic-like, mesenchymal-like, and OPC-like, even at a single-cell level. GFAP+ and βIII tubulin+ cells were readily detectable, suggestive of differentiation of the mGSCs occurring in vivo.

Profiling the immune TME is important for characterizing immunocompetent GBM models and provides a baseline for potentially identifying prognostic features of successful immunotherapy. We used immunohistochemical, FACS, and transcriptomic analyses of tumor-infiltrating immune cells to define distinct immune microenvironment profiles among the mGSC models. Myeloid populations consistently represented a major subset in the TME comprising over 30% of CD45+ cells, recapitulating the dominant presence of bone marrow-derived macrophages in human GBMs.[64,65] On the other hand, infiltration of lymphoid populations into the TME varied markedly between the models. Of note, C1 and C3 tumors had a low proportion of lymphocytes and a high proportion of myeloid cells, compared with 005, RIG, and NF53. Interestingly, C1 and C3 mGSCs had the lowest SNP counts, which is likely associated with a decrease in tumor neo-antigen load. Indeed, the abundance of TILs has been shown to be positively correlated with tumor mutation burden (represented by SNPs) in both cancer patients[66] and murine GBM models.[15,31] This may be relevant therapeutically since baseline TILs have been shown to be a biomarker of immunotherapy responses in some cancers.[67,68] Thus, distinct SNP counts may contribute to the observed heterogeneity in tumor phenotypes and immune microenvironment profiles.

C1 and C3 mGSCs were derived from the same lentivirus construct and mouse strains and have almost the same SNP frequency. However, compared to C1 tumors, C3

tumors have a significantly larger proportion of myeloid cells and MDSCs, and a significantly smaller proportion of TAMs and microglia. Expression of immune checkpoint protein PD-L1 was present in tumor cells, high (>60%) in RIG and C1 and low (~20%) in 005, NF53, and C3. On the other hand, the frequency of PD-L1+ cells was consistently over 80% in all tested myeloid cell types (microglia, TAMs, MDSCs, and DCs) across all the mGSC models. T-cell checkpoint expression, for example, PD-1 and LAG3, was also gained across the models. These findings underscore the immunosuppressive nature of the TME and support the rationale for exploring combination therapies involving immune checkpoint inhibitors.

The broad range of phenotypic diversity between the individual mGSCs and their tumors in immunocompetent mice, despite the same or similar genetic alterations driving initial tumor formation, illustrates the heterogeneity implicit in GBM even within a single tumor. The identification and characterization of cancer stem cells in GBM has resulted in a monumental improvement in our understanding of GBM and has provided representative models to develop and test new therapeutics for GBM.[38,69,70] The prior lack of mGSCs that formed tumors in immunocompetent mice has held back the development and preclinical testing of effective immunotherapies for GBM.[71] The extensive characterization of the panel of mGSC models we report herein should pave the way for future studies that will focus on functional and therapeutic investigations. For example, the NF53 model will provide us with opportunities to probe the role of Pten silencing in tumor invasiveness and infiltration of CD8+ T cells and TAMs. It will be important to characterize the impact of TME factors, such as cytokines and immune checkpoints, on tumor phenotypes. Evaluation of in vivo responses to immunotherapy, such as immune checkpoint blockade and oncolytic viruses,[37] is among our current and future research objectives.

In conclusion, our comprehensive characterization of 5 mGSC models highlights the diversity of tumor phenotypes and immune microenvironment profiles within this subset of GBM cells. These mGSCs are valuable tools for investigating GBM biology and therapeutic strategies, particularly in the context of immunotherapy. The observed heterogeneity underscores the importance of selecting appropriate models for specific research questions and the need for further investigations to unravel the underlying mechanisms driving these distinct phenotypes.

## Supplementary material

Supplementary material is available online at *Neuro-Oncology Advances* (https://academic.oup.com/noa).

## Keywords

GBM | glioblastoma stem-like cells | GSC | immunocompetent GBM model | tumor microenvironment

## Funding

This work was supported in part by a grant from the National Institutes of Health (NIH) (R01 CA160762), the Thomas A. Pappas chair in Neurosciences to S.D.R., and a grant from the American Cancer Society to H.W. M.A.D.A.J. was supported by a National Science Scholarship (MB-PhD) from the Agency for Science, Technology & Research, Singapore, and the John Butterfield Harvard Award from Downing College, University of Cambridge, UK.

## Conflict of interest statement

None declared.

## Acknowledgments

We thank M. Humphrey for maintaining the cell stocks and technical assistance, the HSCI CRM Flow Cytometry Core for FACS technical assistance, the animal facility personnel for assisting with mouse care, Dr. T. Seyfried for providing the CT2A cells, and Dr. Tony Hunter at the Salk Institute for supporting mGSC generation and characterization.

## Author contributions

K.K. performed most of the in vitro and in vivo experiments and wrote and edited the manuscript. S.M.G. performed Flow Cytometry studies and analyses. M.A.D.A.J. performed image analysis and statistical analysis and edited the manuscript. N.R. performed image analysis. J.S.G. assisted with tumor models and FACS. A.S.-R. performed pathological examinations and edited the manuscript. Y.S. generated and provided mGSCs. T.H. generated and provided mGSCs and edited the manuscript. R.L.M. provided clinical expertise, analysis of data, and edited the manuscript. H.W. supervised the work, analyzed data, and wrote and edited the manuscript. S.D.R. designed the overall studies, supervised the work, analyzed data, edited the manuscript, and obtained funding. All authors read and approved the manuscript.

## Data availability

The data supporting the findings of this study are available from the corresponding author on reasonable request.

## Affiliations

Molecular Neurosurgery Laboratory and the Brain Tumor Research Center, and Department of Neurosurgery,

Massachusetts General Hospital and Harvard Medical School, Boston, Massachusetts, USA (K.K., S.M.G., M.A.D.A.J., N.R., J.S.G., R.L.M., H.W., S.D.R.); Department of Pathology, Massachusetts General Hospital and Harvard Medical School, Boston, Massachusetts, USA (A.S.-R., T.H.); Division of Molecular and Medical Genetics, Institute of Medical Science, The University of Tokyo, Minato-ku, Tokyo, Japan (Y.S.); Laboratory of Genetics, Salk Institute for Biological Studies, La Jolla, California, USA (Y.S., T.H.); Center for Cancer Research, Massachusetts General Hospital and Harvard Medical School, Boston, Massachusetts, USA (T.H.);

## References

1. Ostrom QT, Price M, Neff C, et al. CBTRUS statistical report: primary brain and other central nervous system tumors diagnosed in the United States in 2015-2019. *Neuro Oncol.* 2022;24(Suppl 5):v1–v95.
2. Louis DN, Perry A, Wesseling P, et al. The 2021 WHO classification of tumors of the central nervous system: a summary. *Neuro Oncol.* 2021;23(8):1231–1251.
3. Rominiyi O, Vanderlinden A, Clenton SJ, et al. Tumour treating fields therapy for glioblastoma: current advances and future directions. *Br J Cancer.* 2021;124(4):697–709.
4. Wen PY, Weller M, Lee EQ, et al. Glioblastoma in adults: a Society for Neuro-Oncology (SNO) and European Society of Neuro-Oncology (EANO) consensus review on current management and future directions. *Neuro Oncol.* 2020;22(8):1073–1113.
5. Arrieta VA, Dmello C, McGrail DJ, et al. Immune checkpoint blockade in glioblastoma: from tumor heterogeneity to personalized treatment. *J Clin Invest.* 2023;133(2):e163447.
6. Wakimoto H, Mohapatra G, Kanai R, et al. Maintenance of primary tumor phenotype and genotype in glioblastoma stem cells. *Neuro Oncol.* 2012;14(2):132–144.
7. Suvà ML, Tirosh I. The glioma stem cell model in the era of single-cell genomics. *Cancer Cell.* 2020;37(5):630–636.
8. Wakimoto H, Kesari S, Farrell CJ, et al. Human glioblastoma-derived cancer stem cells: establishment of invasive glioma models and treatment with oncolytic herpes simplex virus vectors. *Cancer Res.* 2009;69(8):3472–3481.
9. Esaki S, Nigim F, Moon E, et al. Blockade of transforming growth factor-beta signaling enhances oncolytic herpes simplex virus efficacy in patient-derived recurrent glioblastoma models. *Int J Cancer.* 2017;141(11):2348–2358.
10. Ning J, Wakimoto H, Peters C, Martuza RL, Rabkin SD. Rad51 degradation: role in oncolytic virus-poly(ADP-Ribose) polymerase inhibitor combination therapy in glioblastoma. *J Natl Cancer Inst.* 2017;109(3):1–13.
11. Saha D, Wakimoto H, Peters CW, et al. Combinatorial effects of VEGFR kinase inhibitor axitinib and oncolytic virotherapy in mouse and human glioblastoma stem-like cell models. *Clin Cancer Res.* 2018;24(14):3409–3422.
12. Ning JF, Stanciu M, Humphrey MR, et al. Myc-targeted CDK18 promotes ATR and homologous recombination to mediate PARP inhibitor resistance in glioblastoma. *Nat Commun.* 2019;10(1):2910.
13. Chuprin J, Buettner H, Seedhom MO, et al. Humanized mouse models for immuno-oncology research. *Nat Rev Clin Oncol.* 2023;20(3):192–206.
14. Chen A, Neuwirth I, Herndler-Brandstetter D. Modeling the tumor microenvironment and cancer immunotherapy in next-generation humanized mice. *Cancers (Basel).* 2023;15(11):2989.
15. Ren AL, Wu JY, Lee SY, Lim M. Translational models in glioma immunotherapy research. *Curr Oncol.* 2023;30(6):5704–5718.
16. Ausman JI, Shapiro WR, Rall DP. Studies on the chemotherapy of experimental brain tumors: development of an experimental model. *Cancer Res.* 1970;30(9):2394–2400.
17. Seyfried TN, el-Abbadi M, Roy ML. Ganglioside distribution in murine neural tumors. *Mol Chem Neuropathol.* 1992;17(2):147–167.
18. Johanns TM, Ward JP, Miller CA, et al. Endogenous neoantigen-specific CD8 T cells identified in two glioblastoma models using a cancer immunogenomics approach. *Cancer Immunol Res.* 2016;4(12):1007–1015.
19. Haddad AF, Young JS, Amara D, et al. Mouse models of glioblastoma for the evaluation of novel therapeutic strategies. *Neurooncol Adv.* 2021;3(1):vdab100.
20. Cheema TA, Wakimoto H, Fecci PE, et al. Multifaceted oncolytic virus therapy for glioblastoma in an immunocompetent cancer stem cell model. *Proc Natl Acad Sci U S A.* 2013;110(29):12006–12011.
21. Marumoto T, Tashiro A, Friedmann-Morvinski D, et al. Development of a novel mouse glioma model using lentiviral vectors. *Nat Med.* 2009;15(1):110–116.
22. Hu Y, Smyth GK. ELDA: extreme limiting dilution analysis for comparing depleted and enriched populations in stem cell and other assays. *J Immunol Methods.* 2009;347(1–2):70–78.
23. Angel I, Pilo Kerman O, Rousso-Noori L, Friedmann-Morvinski D. Tenascin C promotes cancer cell plasticity in mesenchymal glioblastoma. *Oncogene.* 2020;39(46):6990–7004.
24. Kiyokawa J, Kawamura Y, Ghouse SM, et al. Modification of extracellular matrix enhances oncolytic adenovirus immunotherapy in glioblastoma. *Clin Cancer Res.* 2021;27(3):889–902.
25. Ning J, Gavil NV, Wu S, et al. Functional virus-specific memory T cells survey glioblastoma. *Cancer Immunol Immunother.* 2022;71(8):1863–1875.
26. Saha D, Martuza RL, Rabkin SD. Macrophage polarization contributes to glioblastoma eradication by combination immunovirotherapy and immune checkpoint blockade. *Cancer Cell.* 2017;32(2):253–267.e5.
27. Amoozgar Z, Kloepper J, Ren J, et al. Targeting Treg cells with GITR activation alleviates resistance to immunotherapy in murine glioblastomas. *Nat Commun.* 2021;12(1):2582.
28. Hong B, Sahu U, Mullarkey MP, et al. PKR induces TGF-beta and limits oncolytic immune therapy. *J ImmunoTher Cancer.* 2023;11(2):e006164.
29. Agemy L, Friedmann-Morvinski D, Kotamraju VR, et al. Targeted nanoparticle-enhanced proapoptotic peptide as potential therapy for glioblastoma. *Proc Natl Acad Sci U S A.* 2011;108(42):17450–17455.
30. Saalik P, Lingasamy P, Toome K, et al. Peptide-guided nanoparticles for glioblastoma targeting. *J Control Release.* 2019;308:109–118.
31. Khalsa JK, Cheng N, Keegan J, et al. Immune phenotyping of diverse syngeneic murine brain tumors identifies immunologically distinct types. *Nat Commun.* 2020;11(1):3912.
32. Cancer Genome Atlas Research Network. Comprehensive genomic characterization defines human glioblastoma genes and core pathways. *Nature.* 2008;455(7216):1061–1068.
33. Friedmann-Morvinski D, Narasimamurthy R, Xia Y, et al. Targeting NF-kappaB in glioblastoma: a therapeutic approach. *Sci Adv.* 2016;2(1):e1501292.
34. Friedmann-Morvinski D, Bushong EA, Ke E, et al. Dedifferentiation of neurons and astrocytes by oncogenes can induce gliomas in mice. *Science.* 2012;338(6110):1080–1084.
35. Saha D, Rabkin SD. Immunohistochemistry for tumor-infiltrating immune cells after oncolytic virotherapy. *Methods Mol Biol.* 2020;2058:179–190.
36. Bommareddy PK, Lowe DB, Kaufman HL, Rabkin SD, Saha D. Multi-parametric flow cytometry staining procedure for analyzing tumor-infiltrating immune cells following oncolytic herpes simplex

virus immunotherapy in intracranial glioblastoma. *J Biol Methods*. 2019;6(2):e112.
37. Kardani K, Sanchez Gil J, Rabkin SD. Oncolytic herpes simplex viruses for the treatment of glioma and targeting glioblastoma stem-like cells. *Front Cell Infect Microbiol*. 2023;13:1206111.
38. Prager BC, Bhargava S, Mahadev V, Hubert CG, Rich JN. Glioblastoma stem cells: driving resilience through chaos. *Trends Cancer*. 2020;6(3):223–235.
39. Tang X, Zuo C, Fang P, et al. Targeting glioblastoma stem cells: a review on biomarkers, signal pathways and targeted therapy. *Front Oncol*. 2021;11:701291.
40. Suva ML, Rheinbay E, Gillespie SM, et al. Reconstructing and reprogramming the tumor-propagating potential of glioblastoma stem-like cells. *Cell*. 2014;157(3):580–594.
41. Beier CP, Beier D. CD133 negative cancer stem cells in glioblastoma. *Front Biosci (Elite Ed)*. 2011;3(2):701–710.
42. He Y, Døssing KBV, Sloth AB, et al. Quantitative evaluation of stem-like markers of human glioblastoma using single-cell RNA sequencing datasets. *Cancers (Basel)*. 2023;15(5):1557.
43. Chen R, Nishimura MC, Bumbaca SM, et al. A hierarchy of self-renewing tumor-initiating cell types in glioblastoma. *Cancer Cell*. 2010;17(4):362–375.
44. Saha D, Rabkin SD, Martuza RL. Temozolomide antagonizes oncolytic immunovirotherapy in glioblastoma. *J ImmunoTher Cancer*. 2020;8(1):e000345.
45. Neftel C, Laffy J, Filbin MG, et al. An integrative model of cellular states, plasticity, and genetics for glioblastoma. *Cell*. 2019;178(4):835–849.e21.
46. Charles NA, Holland EC, Gilbertson R, Glass R, Kettenmann H. The brain tumor microenvironment. *Glia*. 2012;60(3):502–514.
47. Arlauckas SP, Garren SB, Garris CS, et al. Arg1 expression defines immunosuppressive subsets of tumor-associated macrophages. *Theranostics*. 2018;8(21):5842–5854.
48. Tang F, Wang Y, Zeng Y, et al. Tumor-associated macrophage-related strategies for glioma immunotherapy. *Npj Precis Oncol*. 2023;7(1):78.
49. Yang W, Li Y, Gao R, Xiu Z, Sun T. MHC class I dysfunction of glioma stem cells escapes from CTL-mediated immune response via activation of Wnt/β-catenin signaling pathway. *Oncogene*. 2020;39(5):1098–1111.
50. Johnson AL, Laterra J, Lopez-Bertoni H. Exploring glioblastoma stem cell heterogeneity: immune microenvironment modulation and therapeutic opportunities. *Front Oncol*. 2022;12:995498.
51. Wang AZ, Mashimo BL, Schaettler MO, et al. Glioblastoma-infiltrating CD8+ T cells are predominantly a clonally expanded GZMK+ effector population. *Cancer Discov*. 2024;14(6):1106–1131.
52. Yeo AT, Rawal S, Delcuze B, et al. Single-cell RNA sequencing reveals evolution of immune landscape during glioblastoma progression. *Nat Immunol*. 2022;23(6):971–984.
53. Genoud V, Marinari E, Nikolaev SI, et al. Responsiveness to anti-PD-1 and anti-CTLA-4 immune checkpoint blockade in SB28 and GL261 mouse glioma models. *OncoImmunol*. 2018;7(12):e1501137.
54. Chen CH, Chin RL, Hartley GP, et al. Novel murine glioblastoma models that reflect the immunotherapy resistance profile of a human disease. *Neuro Oncol*. 2023;25(8):1415–1427.
55. Kosaka A, Ohkuri T, Okada H. Combination of an agonistic anti-CD40 monoclonal antibody and the COX-2 inhibitor celecoxib induces anti-glioma effects by promotion of type-1 immunity in myeloid cells and T-cells. *Cancer Immunol Immunother*. 2014;63(8):847–857.
56. Reilly KM, Loisel DA, Bronson RT, McLaughlin ME, Jacks T. Nf1;Trp53 mutant mice develop glioblastoma with evidence of strain-specific effects. *Nat Genet*. 2000;26(1):109–113.
57. Zhu Y, Harada T, Liu L, et al. Inactivation of NF1 in CNS causes increased glial progenitor proliferation and optic glioma formation. *Devel (Cambridge, England)*. 2005;132(24):5577–5588.
58. Flores-Toro JA, Luo D, Gopinath A, et al. CCR2 inhibition reduces tumor myeloid cells and unmasks a checkpoint inhibitor effect to slow progression of resistant murine gliomas. *Proc Natl Acad Sci U S A*. 2020;117(2):1129–1138.
59. Trivedi V, Yang C, Klippel K, et al. mRNA-based precision targeting of neoantigens and tumor-associated antigens in malignant brain tumors. *Genome Med*. 2024;16(1):17.
60. Karachi A, Yang C, Dastmalchi F, et al. Modulation of temozolomide dose differentially affects T-cell response to immune checkpoint inhibition. *Neuro Oncol*. 2019;21(6):730–741.
61. Wan F, Zhang S, Xie R, et al. The utility and limitations of neurosphere assay, CD133 immunophenotyping and side population assay in glioma stem cell research. *Brain Pathol*. 2010;20(5):877–889.
62. Clement V, Dutoit V, Marino D, Dietrich PY, Radovanovic I. Limits of CD133 as a marker of glioma self-renewing cells. *Int J Cancer*. 2009;125(1):244–248.
63. Brown DV, Filiz G, Daniel PM, et al. Expression of CD133 and CD44 in glioblastoma stem cells correlates with cell proliferation, phenotype stability and intra-tumor heterogeneity. *PLoS One*. 2017;12(2):e0172791.
64. Klemm F, Maas RR, Bowman RL, et al. Interrogation of the microenvironmental landscape in brain tumors reveals disease-specific alterations of immune cells. *Cell*. 2020;181(7):1643–1660.e17.
65. Pinton L, Masetto E, Vettore M, et al. The immune-suppressive microenvironment of human gliomas depends on the accumulation of bone marrow-derived macrophages in the center of the lesion. *J ImmunoTher Cancer*. 2019;7(1):58.
66. Charoentong P, Finotello F, Angelova M, et al. Pan-cancer immunogenomic analyses reveal genotype-immunophenotype relationships and predictors of response to checkpoint blockade. *Cell Rep*. 2017;18(1):248–262.
67. Chen DS, Mellman I. Elements of cancer immunity and the cancer-immune set point. *Nature*. 2017;541(7637):321–330.
68. Gnjatic S, Bronte V, Brunet LR, et al. Identifying baseline immune-related biomarkers to predict clinical outcome of immunotherapy. *J ImmunoTher Cancer*. 2017;5:44.
69. Yabo YA, Niclou SP, Golebiewska A. Cancer cell heterogeneity and plasticity: a paradigm shift in glioblastoma. *Neuro Oncol*. 2022;24(5):669–682.
70. Silver A, Feier D, Ghosh T, et al. Heterogeneity of glioblastoma stem cells in the context of the immune microenvironment and geospatial organization. *Front Oncol*. 2022;12:1022716.
71. Wouters R, Bevers S, Riva M, De Smet F, Coosemans A. Immunocompetent mouse models in the search for effective immunotherapy in glioblastoma. *Cancers (Basel)*. 2020;13(1):19.